Observation of highly stable and symmetric lanthanide octa-boron inverse sandwich complexes

Wan-Lu Li[a,b,1], Teng-Teng Chen[c,1], Deng-Hui Xing[a,b], Xin Chen[a,b], Jun Li (李 隽)[a,b,2], and Lai-Sheng Wang[c,2]

[a]Department of Chemistry, Tsinghua University, Beijing 100084, China; [b]Key Laboratory of Organic Optoelectronics and Molecular Engineering of Ministry of Education, Tsinghua University, Beijing 100084, China; and [c]Department of Chemistry, Brown University, Providence, RI 02912

Edited by Christopher C. Cummins, Massachusetts Institute of Technology, Cambridge, MA, and approved June 14, 2018 (received for review April 14, 2018)

While boron forms a wide range of metal borides with important industrial applications, there has been relatively little attention devoted to lanthanide boride clusters. Here we report a joint photoelectron spectroscopy and quantum chemical study on two octa-boron di-lanthanide clusters, $Ln_2B_8^-$ (Ln = La, Pr). We found that these clusters form highly stable inverse sandwich structures, $[Ln–B_8–Ln]^-$, with strong Ln and B_8 bonding via interactions between the Ln 5d orbitals and the delocalized σ and π orbitals on the B_8 ring. A (d–p)δ bond, involving the 5dδ and the antibonding π orbital of the B_8 ring, is observed to be important in the Ln–B_8 interactions. The highly symmetric inverse sandwich structures are overwhelmingly more stable than any other isomers. Upon electron detachment, the (d–p)δ orbitals become half-filled, giving rise to a triplet ground state for neutral La_2B_8. In addition to the two unpaired electrons in the (d–p)δ orbitals upon electron detachment, the neutral Pr_2B_8 complex also contains two unpaired 4f electrons on each Pr center. The six unpaired spins in Pr_2B_8 are ferromagnetically coupled to give rise to a septuplet ground state. The current work suggests that highly magnetic Ln…B_8…Ln inverse sandwiches or 1D Ln…B_8…Ln nanowires may be designed with novel electronic and magnetic properties.

lanthanide boride clusters | inverse sandwich | photoelectron spectroscopy | chemical bonding | magnetism

Boron forms a wide variety of boride materials, ranging from the superconductor MgB_2 to superhard transition metal borides (1, 2). In particular, lanthanide borides represent a class of highly valuable magnetic, optical, superconducting, and thermoelectric materials (3–6). In the past two decades, extensive experimental and theoretical studies have been conducted to elucidate the structures and chemical bonding of size-selected boron clusters (7–11), resulting in the discoveries of novel graphene-like (borophene), fullerene-like (borospherene), and nanotubular structures (12–16). However, there has been relatively less attention devoted to metal boride clusters, even though a number of transition metal-doped clusters have been characterized (11, 17–19). In particular, there have been few experimental studies on lanthanide boron clusters.

The SmB_6^- and PrB_7^- clusters represent the first lanthanide (Ln) boron clusters reported (20, 21), each featuring a B_6 or B_7 cluster coordinated to the Ln atom. Here we present a joint photoelectron spectroscopy (PES) and quantum chemical study of the first di-Ln–doped boron clusters, $La_2B_8^-$ and $Pr_2B_8^-$. We have found that these clusters have highly stable and symmetric inverse sandwich structures: a B_8 ring sandwiched by the two Ln atoms, $[Ln–B_8–Ln]^-$. Both anionic complexes are found to have D_{4h} symmetry, whereas upon electron detachment the neutral La_2B_8 and Pr_2B_8 complexes are found to possess perfect D_{8h} symmetry. The interactions between the Ln atoms and the B_8 ring are derived from strong Ln5d and B2p π and δ interactions. The bonding in the Ln_2B_8 inverse sandwich complexes can help us understand the bonding properties of bulk systems and the design of novel lanthanide boride materials.

PES

The experiment was performed using a magnetic-bottle PES apparatus equipped with a laser vaporization supersonic cluster source (10) (see *SI Appendix*, *Methods* for more details). Briefly, lanthanide boron clusters were generated by laser ablation of a La/^{11}B or Pr/^{11}B mixed target, followed by supersonic expansion using a helium carrier gas seeded with 5% argon. Negatively charged clusters were extracted from the cluster beam and analyzed by a time-of-flight mass spectrometer. Clusters with different $La_xB_y^-$ or $Pr_xB_y^-$ compositions were produced. The $La_2B_8^-$ and $Pr_2B_8^-$ clusters of current interest were mass-selected and photodetached by the 193-nm radiation of an ArF excimer laser (6.424 eV). PES data at 193 nm were first obtained for the $La_2B_8^-$ cluster, which was found to exhibit a particularly simple spectral pattern (Fig. 1*A*), suggesting a highly symmetric structure. Subsequently, the spectrum of $Pr_2B_8^-$ was measured (Fig. 1*B*), revealing a similar spectral pattern as $La_2B_8^-$ and indicating that the two di-Ln–octa-boron clusters should have similar structures and bonding.

The two spectra each displayed four well-resolved bands labeled as X, A, B, and C. PES involves electron detachment from the anions, resulting in neutral species. The lowest binding energy band (X) corresponds to detachment transition from the ground state of the $Ln_2B_8^-$ anion to that of the corresponding neutral, whereas bands A, B, and C correspond to detachment transitions to excited states of neutral Ln_2B_8. The broad widths of some of the

Significance

Lanthanide borides constitute an important class of materials with wide industrial applications, but clusters of lanthanide borides have been rarely investigated. It is of great interest to study these nanosystems, which may provide molecular-level understanding of the emergence of new properties and provide insight into designing new boride materials. We have produced lanthanide boride clusters and probed their electronic structure and chemical bonding. Two $Ln_2B_8^-$ clusters are presented, and they are found to possess inverse sandwich structures. The neutral Ln_2B_8 complexes are found to possess D_{8h} symmetry with strong Ln–B_8 bonding. A unique (d–p)δ bond is found to be important for the Ln–B_8–Ln interactions. The Ln_2B_8 inverse sandwich complexes broaden the structural chemistry of the lanthanide elements and provide insights into bonding in lanthanide boride materials.

Author contributions: J.L. and L.-S.W. designed research; W.-L.L., T.-T.C., D.-H.X., and X.C. performed research; W.-L.L. and T.-T.C. analyzed data; and W.-L.L., T.-T.C., J.L., and L.-S.W. wrote the paper.

The authors declare no conflict of interest.

This article is a PNAS Direct Submission.

[1]W.-L.L. and T.-T.C. contributed equally to this work.

[2]To whom correspondence may be addressed. Email: junli@tsinghua.edu.cn or Lai-Sheng_Wang@Brown.edu.

This article contains supporting information online at www.pnas.org/lookup/suppl/doi:10.1073/pnas.1806476115/-/DCSupplemental.

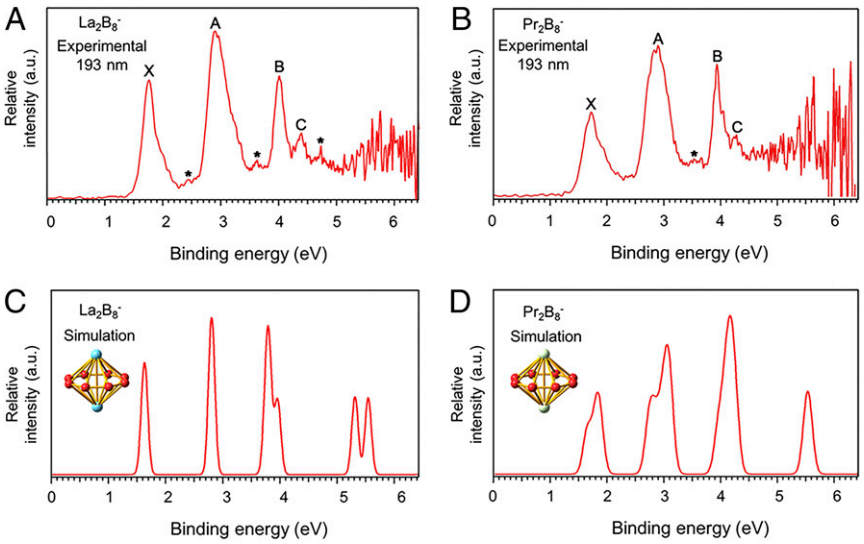

Fig. 1. Photoelectron spectra of (*A*) $La_2B_8^-$ and (*B*) $Pr_2B_8^-$ at 193 nm and comparison with the simulated spectra for the (*C*) D_{4h} $La_2B_8^-$ and (*D*) D_{4h} $Pr_2B_8^-$. See *SI Appendix*, Tables S4 and S5 for the detachment energies of the observed bands and their assignments for $La_2B_8^-$ and $Pr_2B_8^-$, respectively.

detachment bands suggest that they may contain multiple detachment transitions. The X band yielded the first vertical detachment energy (VDE) of 1.76 eV for $La_2B_8^-$ and 1.75 eV for $Pr_2B_8^-$. The adiabatic detachment energy (ADE) for band X was evaluated from its onset to be 1.64 ± 0.05 eV and 1.59 ± 0.05 eV, which represent the electron affinities (EAs) of neutral La_2B_8 and Pr_2B_8, respectively. The A band at 2.91 eV ($La_2B_8^-$) and 2.94 eV ($Pr_2B_8^-$) was broad and intense in both spectra. At around 4 eV, both spectra displayed a relatively sharp band B, closely followed by a weak band C. The signal/noise ratios above 5 eV were poor, and no specific detachment bands could be definitively identified. Some weak features appeared around bands A and B and also possibly above band C (labeled by *). These weak features were likely due to multielectron or shakeup processes, as a result of strong electron correlation effects expected for these systems (22). The well-resolved photoelectron spectral features served as electronic fingerprints to allow analyses of their structures and bonding by comparing with theoretical calculations.

Global Minimum Structure Searches

$La_2B_8^-$. The global minimum structure for $La_2B_8^-$ was searched using the Tsinghua Global Minimum (TGMin) package (23, 24) with a constrained basin-hopping algorithm (25) (see *SI Appendix*, *Methods* for the computational details). A D_{4h} ($^2B_{2u}$) inverse sandwich structure was found to be the global minimum (*SI Appendix*, Fig. S1). The D_{4h} structure of the $La_2B_8^-$ anion was distorted from the perfect D_{8h} symmetry due to the Jahn–Teller effect. We optimized the neutral D_{4h} La_2B_8, which led to the perfect D_{8h} ($^3A_{2g}$) structure, as shown in Fig. 2. The structural differences between the anion and neutral are relatively small. The coordinates of the anion and neutral global minima are given in *SI Appendix*, Table S1. For the first two isomers, CCSD(T) calculations with the PBE0/TZP geometries were further carried out to obtain more accurate relative energies. The CCSD(T) results were deemed reliable because the multiconfigurational characters were not significant from the T_1 diagnostic factors of CCSD calculations (0.018 for the global minimum of $La_2B_8^-$).

The closest isomer above the global minimum had C_s symmetry (*SI Appendix*, Fig. S1), which was 32.41 kcal/mol higher in energy at the CCSD(T) level, indicating the overwhelmingly high stability of the D_{4h} symmetrical inverse sandwich structure. The isomer of $La_2B_8^-$ with a seven-atom ring and one B atom squeezed out was found to be the third isomer, which lies 36.37 kcal/mol above the global minimum at the PBE0/TZP level. The isomer with a pseudoC_{7v} B©B_7 moiety (the most stable structure for bare B_8) (26), sandwiched by the two La atoms, is even higher in energy (67.07 kcal/mol at the PBE0/TZP level).

$Pr_2B_8^-$. On the basis of their similar PE spectra, we expected that $Pr_2B_8^-$ should have a similar global minimum as $La_2B_8^-$. Indeed, we found that $Pr_2B_8^-$ has a D_{4h} structure with a sextet ground state ($^6B_{2u}$). Neutral Pr_2B_8 upon electron detachment was found to have a perfect D_{8h} symmetry with six unpaired electrons ($^7A_{2g}$). The structural parameters for the D_{8h} Pr_2B_8 are also shown in Fig. 2, together with those of La_2B_8, and its coordinates are given in the *SI Appendix*, Table S2. We have obtained preliminary PES data for a late lanthanide, $Tb_2B_8^-$ (*SI Appendix*, Fig. S2), which also gives a similar spectral pattern as those of $La_2B_8^-$ and $Pr_2B_8^-$. Hence, we expect that many lanthanide elements may form the highly symmetric Ln–B_8–Ln inverse sandwich structures, as confirmed for $La_2B_8^-$ and $Pr_2B_8^-$ by comparison between experiment and theory.

Comparison Between the Experimental and Computational Results

To validate the global minima of $La_2B_8^-$ and $Pr_2B_8^-$, we calculated their ADEs and VDEs using the ΔSCF–TDDFT formalism. Fig. 1 *C* and *D* present the simulated spectra for the D_{4h} global

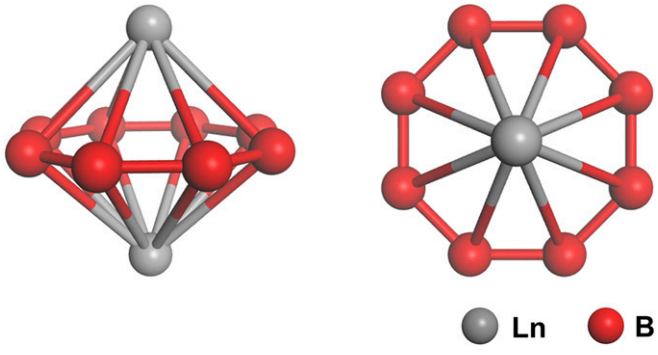

Fig. 2. Two views of the global minima of the neutral D_{8h} Ln_2B_8. Bon lengths: Ln. . .Ln = 3.720 Å (La), 3.558 Å (Pr); Ln–B = 2.759 Å (La), 2.701 Å (Pr); B–B = 1.560 Å (La), 1.555 Å (Pr) at the PBE0/TZP level.

minimum structures, showing excellent agreement with the experimental spectral patterns. The computed ADE/VDEs at the CCSD(T) level are 1.47/1.52 eV and 1.53/1.64 eV for $La_2B_8^-$ and $Pr_2B_8^-$, respectively, in good agreement with the experimental data of 1.64/1.76 eV and 1.59/1.75 eV (*SI Appendix*, Table S3). All of the computed detachment channels for $La_2B_8^-$ and $Pr_2B_8^-$ (including the electron configurations and final state symmetries) and their comparison with the experimental data are given in *SI Appendix*, Tables S4 and S5, respectively. As expected, each observed PES band corresponds to multiple detachment channels.

According to the valence molecular orbital (MO) correlation diagram of La_2B_8 and $La_2B_8^-$ (*SI Appendix*, Fig. S3) and the MO contours of the $La_2B_8^-$ anion (*SI Appendix*, Fig. S4), the bonding patterns of the neutral and anion species are similar. The lower symmetry of the anion is due to the Jahn–Teller effect, as a result of the extra electron in the $1e_{2u}$ MO ($1e_{2u}^3$) in a D_{8h} anion, leading to the slight distortion to the D_{4h} symmetry. Electron detachments from the primarily 5d-type $1b_{2u}$ and $1b_{1u}$ MOs of $La_2B_8^-$ give rise to three detachment channels with very close computed VDEs from 1.597 to 1.661 eV, corresponding to the X band in the PE spectrum (Fig. 1*C* and *SI Appendix*, Table S4). The remaining MOs are all B_8 ring-based fully occupied σ and π orbitals. Detachments from the $4e_u$ and $2e_g$ MOs give rise to four detachment channels with close computed VDEs from 2.798 to 2.856 eV, corresponding well to the A band around 3 eV. Detachments from the $4a_{1g}$ and $3a_{2u}$ MOs give rise to band B, whereas detachment from the $1a_{2g}$ MO gives rise to the weaker band C.

The MOs of $Pr_2B_8^-$ are similar to those of $La_2B_8^-$, except the two half-filled 4f-based $5e_u$ and $3e_g$ MOs (*SI Appendix*, Fig. S5), which contributed to the broad A band (*SI Appendix*, Table S5). Other detachment channels and assignments of $Pr_2B_8^-$ are similar to those of $La_2B_8^-$. Overall, the theoretical VDEs from the D_{4h} $La_2B_8^-$ and $Pr_2B_8^-$ and the simulated PE spectra agree well with the experimental data, providing considerable credence for the identified D_{4h} global minima for the anions and the D_{8h} global minima for the two Ln_2B_8 neutral complexes.

The High Stability of the Ln_2B_8 Inverse Sandwich Complexes

Inverse sandwich structures represent a fascinating class of inorganic compounds, consisting of two metal atoms sandwiching an aromatic hydrocarbon molecule (27–35). The central aromatic molecule forms interesting chemical bonds to the metals on both sides of the molecular plane. Specifically, a δ-bond has been identified to be critical for the arene-bridged diuranium inverse sandwich complexes (32–34). The current $La_2B_8^-$ and $Pr_2B_8^-$ species are the first inverse sandwich structures observed for lanthanide borides. Because of the high symmetry of the corresponding neutral species, we will use the neutral Ln_2B_8 to discuss the stability and bonding of the lanthanide boron inverse sandwiches. The Ln–B bond lengths are around 2.70–2.76 Å (Fig. 2), indicating strong bonding between the Ln and the boron atoms. The Ln–B_8–Ln binding energies calculated for $Ln_2B_8 \rightarrow 2Ln + B_8$ are quite large, 403.89 kcal/mol for La_2B_8 and 456.16 kcal/mol for Pr_2B_8 (*SI Appendix*, Table S6). It should be reiterated that the B_8 ring in the Ln_2B_8 inverse sandwiches is quite different from the bare B_8 cluster, which has a D_{7h} B©B_7 wheel structure (26). The isomer involving this B_8 wheel is much higher in energy, 67.07 kcal/mol above the global minimum (*SI Appendix*, Fig. S1).

Chemical Bonding in the Inverse Sandwich Ln_2B_8 Complexes

Localized MO Analysis in the B_8 Ring. Due to the similarity in the electronic structure and bonding between the anion and neutral species (*SI Appendix*, Fig. S3), we chose the more symmetric neutrals (D_{8h}) to discuss the chemical bonding in the inverse sandwiches. We first analyzed the B_8 ring using the localized coordinate system (Fig. 3). The 32 2s–2p valence orbitals of B_8 can be divided into four categories using a Hückel-type approach—σ_s, $\sigma(t)_p$, $\sigma(r)_p$, and π_p—where "t" and "r" denote tangential and radial bonding, respectively. The occupied σ_s and $\sigma(t)_p$ orbitals constitute the eight B–B bonds in the B_8 ring. Of particular importance are the two sets of delocalized $\sigma(r)_p$ and π_p orbitals, which primarily participate in bonding with the two Ln atoms above and below the B_8 ring. These two sets of orbitals have smaller energy-level splitting because of less overlap between the B atoms as a result of the relatively large ring size (~4.2 Å).

Bonding in La_2B_8 and Ln_2B_8. Fig. 4 presents the MO correlation diagram of La_2B_8 derived from the La…La and B_8 moieties. The

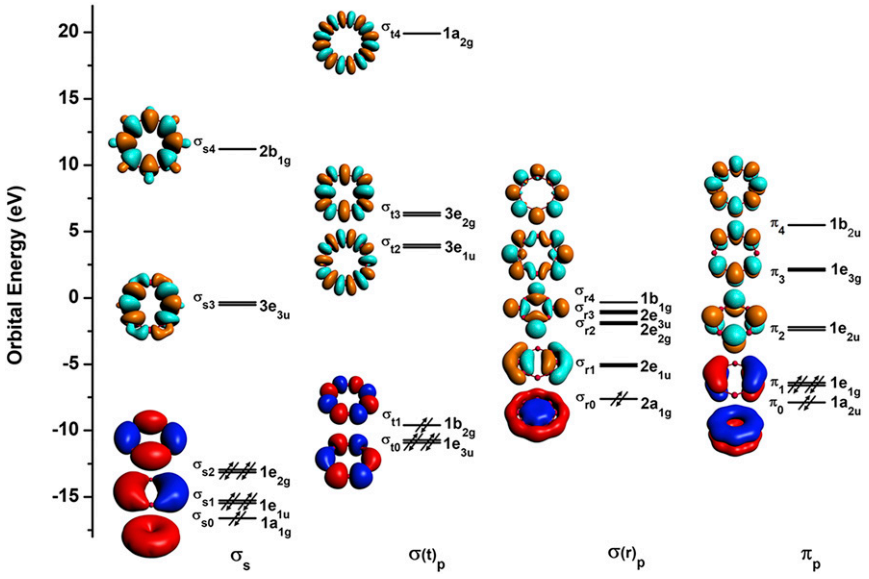

Fig. 3. The localized coordinate system (LCS) of the B_8 moiety from PBE/DZP calculations. The 32 valence orbitals are divided into four types: σ_s, $\sigma(t)_p$, $\sigma(r)_p$, and π_p. The "t" means tangential and "r" means radial. The σ and π orbitals are labeled with a subscript number from 0–4 according to the number of their orbital nodes. The orbital occupancy is also indicated. The occupied and unoccupied orbitals are color-coded.

exceptional stability of La_2B_8 is evident by the large energy gap between the HOMO ($1e_{2u}$) and LUMO ($5a_{1g}$). The 4f orbitals are well known to be radially too contracted in lanthanide elements to participate in chemical bonding. They form a nonbonding f-band in between the HOMO–LUMO region, giving rise to interesting magnetic properties for the Ln_2B_8 complexes (for Ln > La). The Ln 5d orbitals are much more extended than the 4f orbitals radially. Thus, the $5d_\pi$ and 5dδ orbitals of the two Ln atoms are significantly stabilized via bonding with the σ_1 and π_2 orbitals of the B_8 ring. Chemical bonding of the anionic $Ln_2B_8^-$ and neutral Ln_2B_8 differs only in the electron occupation in the $1e_{2u}$ HOMO: It is half-filled ($1e_{2u}^2$) in the neutral, whereas it has a $1e_{2u}^3$ occupation in the anion. Thus, the symmetry of $Ln_2B_8^-$ is reduced from D_{8h} to D_{4h} due to the Jahn–Teller effect, and the $1e_{2u}$ orbital is split to $1b_{2u}$ and $1b_{1u}$ under D_{4h} symmetry (*SI Appendix*, Table S7). The occupied valence MOs for $La_2B_8^-$ and $Pr_2B_8^-$ are shown, respectively, in *SI Appendix*, Figs. S4 and S5. Our bonding analyses will focus on the more symmetric neutral Ln_2B_8.

In La_2B_8, the two La atoms provide four electrons to fill the σ_{r1} orbital of B_8, which is transformed to the $3e_{1u}$ MO in La_2B_8 (Fig. 4). This (d–p)π type bonding orbital contributes the most (74.6%) to the total orbital interactions between La...La and B_8, as revealed through EDA–NOCV analyses [see $\Delta E_{orb(1)}$ and $\Delta E_{orb(1)}'$ in *SI Appendix*, Table S8]. The La...La d–σ_g orbital interacts with the σ_{r0} of B_8 to form the $4a_{1g}$ (d–p)σ MO, which only accounts for 2.2% of the total bonding [see $\Delta E_{orb(3)}$ in *SI Appendix*, Table S8]. The d–π_g orbital of La...La only bonds marginally with the π_1 orbital of B_8 due to symmetry compatibility, accounting for 2.6% of the orbital interactions [see $\Delta E_{orb(4)}$ and $\Delta E_{orb(4)}'$ in *SI Appendix*, Table S8]. Remarkably, the d–δ_u orbital of La...La and the π_2 orbital of B_8 are significantly stabilized because of favorable energy matching and effective orbital overlap to form the $1e_{2u}$ bonding MO occupied with two unpaired electrons. This bond is reminiscent of the δ bond that plays a key role in stabilizing diuranium inverse sandwiches (32–34). This unique (d–p)δ bond is also important for the La_2B_8 inverse sandwich, contributing 17.6% to the total orbital interactions [see $\Delta E_{orb(2)}$ and $\Delta E_{orb(2)}'$ in *SI Appendix*, Table S8].

The bonding patterns are similar in all Ln_2B_8 inverse sandwich complexes, albeit a different number of 4f electrons will give rise to different magnetic properties. The total charge and spin densities of both the anion and neutral Ln_2B_8 species were computed using several methods (*SI Appendix*, Table S9). The spin densities indicate that each Pr holds two unpaired 4f electrons, while no 4f electron is on La. The B atoms also have spin densities because of the two unpaired electrons in the (d–p)δ bonding orbitals. Upon one electron detachment from the $1b_{1u}$ orbital of (d–p)δ character, the reduction of electrons on Ln is more than that on the B atoms, suggesting that the (d–p)δ bond is contributed slightly more by the Ln–5d orbitals. The B_8 ring acts as a doubly aromatic motif to form the inverse sandwich Ln–B_8–Ln complexes. Interestingly, we found some non-negligible Ln...Ln interactions via the σ and π delocalized orbitals of the B_8 ring (*SI Appendix*, Table S6). The distance between the two Ln atoms is about 3.6~3.7 Å, which is remarkably close to the Ln–Ln single bond length (3.60 Å for La–La and 3.52 Å for Pr–Pr based on the self-consistent covalent radii of Pyykkö) (36).

AdNDP Bonding Analysis. The chemical bonding in Ln_2B_8 can be further understood using AdNDP analyses (37), as shown in Fig. 5 for La_2B_8. The AdNDP results show clearly eight two-center two-electron (2c–2e) bonds in the B_8 ring. The remaining bonds are all delocalized 10c–2e bonds. The three delocalized bonds in the first row represent in-plane σ bonds within the B_8 ring involving interactions with the La 5dσ/π orbitals. These bonds give rise to σ aromaticity because they fulfill the Hückel $4N+2$ rule. The five delocalized bonds in the second row represent π bonds in Ln_2B_8, giving rise to π aromaticity for triplet states (38), because of the two single-electron bonds corresponding to the two singly occupied (d–p)δ MOs. Adding two electrons to these MOs would result in a filled (d–p)δ bonding MO and a closed-shell $La_2B_8^{2-}$ with 10 π electrons. The B2p orbitals and the Ln4f orbitals are close in energy. This energetic factor and the fact that boron has low electronegativity make it difficult for Pr or other Ln elements with 4f electrons to donate more electrons to the B_8 ring to fill the (d–p)δ bonding MOs. Hence, even though Pr is

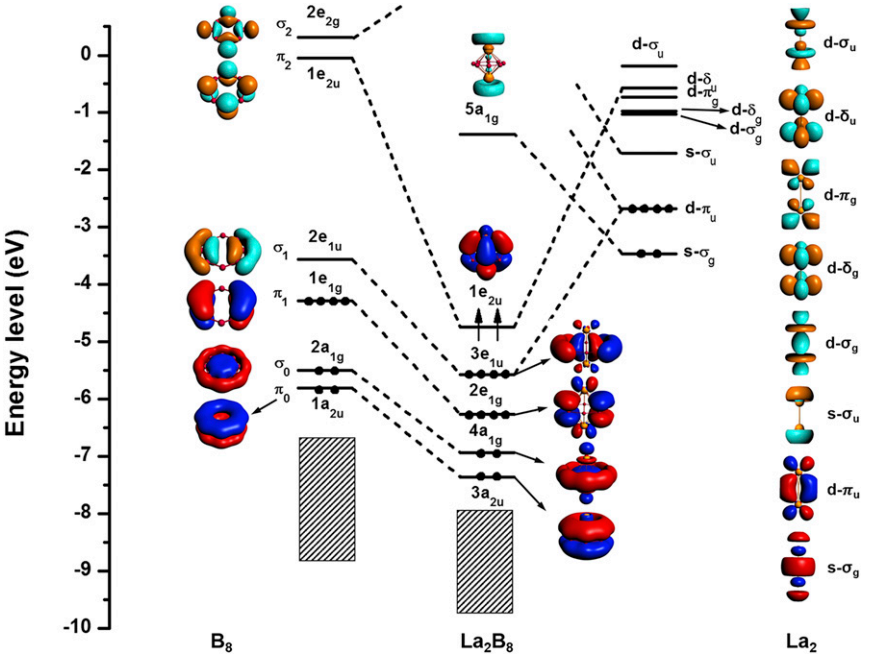

Fig. 4. The MO bonding scheme of D_{8h} La_2B_8 at the level of PBE0/TZP, illustrating the bonding interactions between the La...La and B_8 fragments.

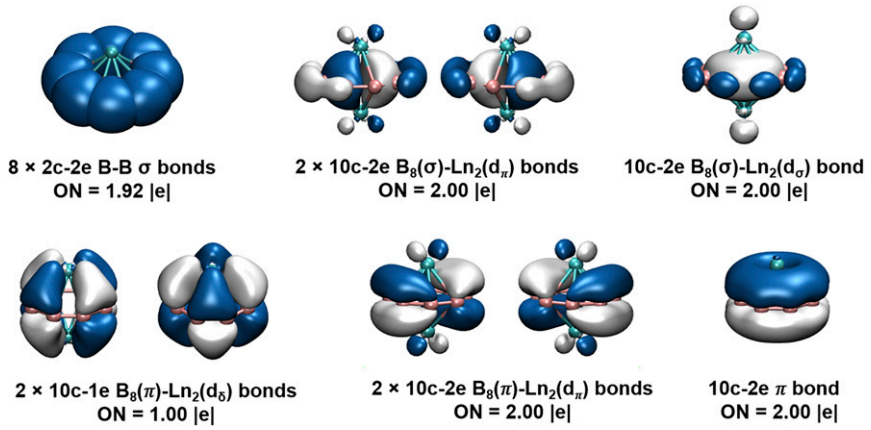

Fig. 5. AdNDP bonding analyses for La_2B_8 at the PBE0/cc-pVTZ level. Occupation numbers (ON) are shown.

known to reach a maximum oxidation state of +V with highly electronegative elements (39), in the Pr_2B_8 inverse sandwich complex each Pr center still retains two 4f electrons (*SI Appendix*, Fig. S5).

Magnetism in La_2B_8 and Pr_2B_8

The La_2B_8 inverse sandwich is magnetic due to the two unpaired electrons in the (d–p)δ (e_{2u}) orbitals. Ferromagnetism was observed in La-doped CaB_6 crystals at high temperatures (40) and has stimulated intense interests due to the many fundamental issues associated with this novel phenomenon (41–43). The divalent CaB_6 is a semiconductor with a band gap of ∼1 eV (44). The observed ferromagnetism in La-doped CaB_6 is due to the partially filled impurity band formed by the La 5d orbitals (45), analogous to the half-filled (d–p)δ orbitals in La_2B_8.

The Pr_2B_8 inverse sandwich has more complicated and interesting magnetic properties due to the partially filled 4f shells. We carried out a series of calculations to determine the electron configurations and spin states of $Pr_2B_8^-$ and Pr_2B_8 (*SI Appendix*, Table S10). The isomers with the promotion of a 4f electron to the 5d orbital, …(d–p)δ^2Pr($4f^2$)Pr($4f^2$), is energetically preferable to the isomer with the …(d–p)δ^4Pr($4f^1$)Pr($4f^1$) configuration by 42.77 kcal/mol at the CCSD(T)/VTZ level. Thus, the bonding in Pr_2B_8 remains the same as in La_2B_8, as discussed above. We also examined the relative energies of possible ferromagnetic and antiferromagnetic configurations and found that the state with septuplet multiplicity is most favorable energetically with the two unpaired electrons in the (d–p)δ bonding MO and the four 4f electrons ferromagnetically coupled. The corresponding antiferromagnetic state (triplet) lies 12.12 kcal/mol higher in energy, calculated using the PBE0/TZP broken-symmetry approach. As expected, the energy differences are small for different occupations of the 4f manifold of orbitals (*SI Appendix*, Table S10). For example, the energy difference between the septuplet …(d–p)δ^2Pr(4fδ^2)Pr(4fδ^2) and septuplet …(d–p)δ^2Pr(4fϕ^2)Pr(4fϕ^2) configurations is only 4.99 kcal/mol at the PBE0 level.

The above single-configurational theoretical results are further examined using the wavefunction theory in the ab initio multiconfigurational framework. State-averaged CASSCF calculations indicate that the ground state of Pr_2B_8 is dominated by the …(d–p)δ^2Pr($4f^2$)Pr($4f^2$) configuration (CI weight: ∼98%), even though the four 4f electrons distribute on almost every type of the near-degenerate 4f orbitals. The corresponding antibonding (d–p)δ* natural orbitals are shown to have occupation numbers only on the order of 0.03 (*SI Appendix*, Fig. S6). The CASPT2 results (*SI Appendix*, Table S11) confirm the septuplet ground state with a CI weight of 94%, which has two unpaired 4fδ and 4fϕ electrons on each Pr atom and two electrons in the degenerate singly occupied (d–p)δ bonding orbitals coupled ferromagnetically. Other calculations based on different occupation situations in the 4f orbitals were further performed. Overall, the septuplet …(d–p)δ^2Pr($4f^2$)Pr($4f^2$) configuration is favored, no matter which type of 4f orbitals is occupied within an energy range of 5 kcal/mol (*SI Appendix*, Table S11). The triplet state dominated by the …(d–p)δ^4Pr($4f^1$)Pr($4f^1$) configuration has shorter Pr…Pr distance (3.30 Å at the PBE0/TZP level) due to the enhanced (d–p)δ bonding, but it lies 38.79 kcal/mol higher in energy than the …(d–p)δ^2Pr($4f^2$)Pr($4f^2$) septuplet ground state.

The antiferromagnetic coupling exhibits strong multiconfigurational characters due to configuration mixing. The lowest antiferromagnetic triplet excited state with two spin-up and two spin-down 4f electrons was evaluated to be 8.73 kcal/mol higher in energy than the septuplet ground state from the CASPT2 calculation (*SI Appendix*, Table S11). The ferromagnetic coupling in the Pr_2B_8 inverse sandwich involves the two f^2 centers and the (d–p)δ bonding diradical $(e_{2u})^2$ on the central B_8 ring, which is highly unusual and is quite different from most Ln compounds with only Ln-centered unpaired spins. We further calculated the relative energies of a ferromagnetic and an antiferromagnetic 1D chain using the periodic VASP code with constrained D_{8h} Pr…B_8…Pr repeating units. The ferromagnetic coupling is found to be more favorable by 11.90 kcal/mol, with nearly 2 μ_b magnetization on each Pr atom and the B_8 ring. If such a highly magnetic nanowire can be realized, it could have potential applications in magnetoresistance or quantum computing, in particular for the Gd…B_8…Gd system with seven f electrons per Gd.

Conclusion

In conclusion, we report the first di-lanthanide octa-boron inverse sandwich complexes. The photoelectron spectra of two representative systems, $Ln_2B_8^-$ (Ln = La, Pr), show similar and relatively simple spectral patterns, suggesting that they have similar high-symmetry structures. Theoretical calculations showed that the $Ln_2B_8^-$ anions have D_{4h} symmetry due to the Jahn–Teller effects, whereas the neutral Ln_2B_8 complexes have perfect D_{8h} symmetry. Strong chemical bonding is found between the Ln atoms and the 2*s* and 2*p* MOs of the B_8 ring. Neutral La_2B_8 has a triplet ground state, displaying diradical characters on the B_8 ring, whereas Pr_2B_8 carries six unpaired spins with each Pr atom retaining two 4*f* electrons. The ground state of Pr_2B_8 is ferromagnetically coupled to give a septuplet spin state. All Ln_2B_8 complexes are expected to display similar structures and bonding, providing opportunities to design highly magnetic Ln_2B_8 sandwich complexes, as well as 1D magnetic nanowires.

ACKNOWLEDGMENTS. The calculations were performed using supercomputers at Tsinghua National Laboratory for Information Science and Technology and the Supercomputing Center, Computer Network Information Center of the Chinese Academy of Sciences. The experimental work at Brown University was supported by National Science Foundation Grant CHE-1763380. The theoretical work at Tsinghua University was supported by National Natural Science Foundation of China Grants 21590792, 91426302, and 21433005.

1. Nagamatsu J, Nakagawa N, Muranaka T, Zenitani Y, Akimitsu J (2001) Superconductivity at 39 K in magnesium diboride. *Nature* 410:63–64.
2. Chung HY, et al. (2007) Synthesis of ultra-incompressible superhard rhenium diboride at ambient pressure. *Science* 316:436–439.
3. Scheifers JP, Zhang Y, Fokwa BPT (2017) Boron: Enabling exciting metal-rich structures and magnetic properties. *Acc Chem Res* 50:2317–2325.
4. Sussardi A, Tanaka T, Khan AU, Schlapbach L, Mori T (2015) Enahnced thermoelectric properties of samarium boride. *J Materiomics* 1:196–204.
5. Akopov G, Yeung MT, Kaner RB (2017) Rediscovering the crystal chemistry of borides. *Adv Mater* 29:1604506.
6. Carenco S, Portehault D, Boissière C, Mézailles N, Sanchez C (2013) Nanoscaled metal borides and phosphides: Recent developments and perspectives. *Chem Rev* 113: 7981–8065.
7. Zhai HJ, Wang LS, Alexandrova AN, Boldyrev AI (2002) Electronic structure and chemical bonding of B_5^- and B_5 by photoelectron spectroscopy and ab initio calculations. *J Chem Phys* 117:7917–7924.
8. Alexandrova AN, Boldyrev AI, Zhai HJ, Wang LS (2006) All-boron aromatic clusters as potential new inorganic ligands and building blocks in chemistry. *Coord Chem Rev* 250:2811–2866.
9. Sergeeva AP, et al. (2014) Understanding boron through size-selected clusters: Structure, chemical bonding, and fluxionality. *Acc Chem Res* 47:1349–1358.
10. Wang LS (2016) Photoelectron spectroscopy of size-selected boron clusters: From planar structures to borophenes and borospherenes. *Int Rev Phys Chem* 35:69–142.
11. Li WL, Chen X, Jian T, Chen TT, Li J, Wang LS (2017) From planar boron clusters to borophenes and metalloborophenes. *Nat Rev Chem* 1:0071.
12. Piazza ZA, et al. (2014) Planar hexagonal $B_{(36)}$ as a potential basis for extended single-atom layer boron sheets. *Nat Commun* 5:3113.
13. Zhai HJ, et al. (2014) Observation of an all-boron fullerene. *Nat Chem* 6:727–731.
14. Kiran B, et al. (2005) Planar-to-tubular structural transition in boron clusters: B_{20} as the embryo of single-walled boron nanotubes. *Proc Natl Acad Sci USA* 102:961–964.
15. Oger E, et al. (2007) Boron cluster cations: Transition from planar to cylindrical structures. *Angew Chem Int Ed Engl* 46:8503–8506.
16. Popov IA, Jian T, Lopez GV, Boldyrev AI, Wang LS (2015) Cobalt-centred boron molecular drums with the highest coordination number in the CoB_{16}^- cluster. *Nat Commun* 6:8654.
17. Romanescu C, Galeev TR, Li WL, Boldyrev AI, Wang LS (2013) Transition-metal-centered monocyclic boron wheel clusters ($M©B_n$): A new class of aromatic borometallic compounds. *Acc Chem Res* 46:350–358.
18. Li WL, et al. (2017) Observation of a metal-centered B_2-Ta@B_{18}^- tubular molecular rotor and a perfect Ta@B_{20}^- boron drum with the record coordination number of twenty. *Chem Commun (Camb)* 53:1587–1590.
19. Jian T, et al. (2016) Competition between drum and quasi-planar structures in RhB_{18}^-: Motifs for metallo-boronanotubes and metallo-borophenes. *Chem Sci (Camb)* 7: 7020–7027.
20. Robinson PJ, Zhang X, McQueen T, Bowen KH, Alexandrova AN (2017) SmB_6^- cluster anion: Covalency involving f orbitals. *J Phys Chem A* 121:1849–1854.
21. Chen TT, et al. (2017) PrB_7^-: A praseodymium-doped boron cluster with a Pr^{II} center coordinated by a doubly aromatic planar η^7-B_7^{3-} ligand. *Angew Chem Int Ed Engl* 56: 6916–6920.
22. Li WL, et al. (2014) Strong electron correlation in $UO_2(-)$: A photoelectron spectroscopy and relativistic quantum chemistry study. *J Chem Phys* 140:094306.
23. Zhao Y, Chen X, Li J (2017) TGMin: A global-minimum structure search program based on a constrained basin-hopping algorithm. *Nano Res* 10:3407–3420.
24. Chen X, Zhao YF, Wang LS, Li J (2017) Recent progresses of global minimum searches of nanoclusters with a constrained basin-hopping algorithm in the TGMin program. *Comput Theor Chem* 1107:57–65.
25. Goedecker S (2004) Minima hopping: An efficient search method for the global minimum of the potential energy surface of complex molecular systems. *J Chem Phys* 120:9911–9917.
26. Zhai HJ, Alexandrova AN, Birch KA, Boldyrev AI, Wang LS (2003) Hepta- and octacoordinate boron in molecular wheels of eight- and nine-atom boron clusters: Observation and confirmation. *Angew Chem Int Ed Engl* 42:6004–6008.
27. Duff AW, Jonas K (1983) The first triple-decker sandwich with a bridging benzene ring. *J Am Chem Soc* 105:5479–5480.
28. Schier A, Wallis JM, Müller G, Schmidbaur H (1986) $[C_6H_3(CH_3)_3][BiCl_3]$ and $[C_6(CH_3)_6][BiCl_3]_2$, arene complexes of bismuth with half-sandwich and "inverted" sandwich structures. *Angew Chem Int Ed Engl* 25:757–759.
29. Streitwieser A, Smith KA (1988) Inverse sandwich compounds. *J Mol Struct THEOCHEM* 163:259–265.
30. Arliguie T, Lance M, Nierlich M, Vigner J, Ephritikhine M (1994) Inverse cycloheptatrienyl sandwich complexes. Crystal structure of $[U(BH_4)_2(OC_4H_8)_5][(BH_4)_3U(\mu\text{-}\eta^7, \eta^7\text{-}C_7H_7)U(BH_4)_3]$. *J Chem Soc Chem Commun,* 847–848.
31. Krieck S, Görls H, Yu L, Reiher M, Westerhausen M (2009) Stable "inverse" sandwich complex with unprecedented organocalcium(I): Crystal structures of [(thf)$_{(2)}$Mg(Br)-C$_{(6)}$H$_{(2)}$-2,4,6-Ph$_{(3)}$] and [(thf)(3)Camu-C(6)H(3)-1,3,5-Ph(3)Ca(thf)(3)]. *J Am Chem Soc* 131:2977–2985.
32. Diaconescu PL, Arnold PL, Baker TA, Mindiola DJ, Cummins CC (2000) Arene-bridged diuranium complexes: Inverted sandwiches supported by δ backbonding. *J Am Chem Soc* 122:6108–6109.
33. Diaconescu PL, Cummins CC (2002) Diuranium inverted sandwiches involving naphthalene and cyclooctatetraene. *J Am Chem Soc* 124:7660–7661.
34. Gardner BM, et al. (2015) An inverted-sandwich diuranium μ-η^5:η^5-cyclo-P_5 complex supported by U-P_5 δ-bonding. *Angew Chem Int Ed Engl* 54:7068–7072.
35. Liddle ST (2015) Inverted sanwich arene complexes of uranuium. *Coord Chem Rev* 293-294:211–227.
36. Pyykkö P (2015) Additive covalent radii for single-, double-, and triple-bonded molecules and tetrahedrally bonded crystals: A summary. *J Phys Chem A* 119:2326–2337.
37. Zubarev DY, Boldyrev AI (2008) Developing paradigms of chemical bonding: Adaptive natural density partitioning. *Phys Chem Chem Phys* 10:5207–5217.
38. Baird NC (1972) Quantum organic photochemistry. II. Resonance and aromaticity in the lowest $^3\pi\pi^*$ state of cyclic hydrocarbons. *J Am Chem Soc* 94:4941–4948.
39. Hu SX, et al. (2017) Pentavalent lanthanide nitride-oxides: NPrO and $NPrO^-$ complexes with N≡Pr triple bonds. *Chem Sci (Camb)* 8:4035–4043.
40. Young DP, et al. (1999) High-temperature weak ferromagnetism in a low-density free-electron gas. *Nature* 397:412–414.
41. Fisk Z, Otto HR, Barzykin V, Gor'kov LP (2002) The emerging picture of ferromagnetism in the divalent hexaborides. *Physica B* 312-313:808–810.
42. Sun L, Wu Q (2016) Pressure-induced exotic states in rare earth hexaborides. *Rep Prog Phys* 79:084503.
43. Hartstein M, et al. (2018) Fermi surface in the absence of a Fermi liquid in the Kondo insulator SmB_6. *Nat Phys* 14:166–172.
44. Denlinger JD, et al. (2002) Bulk band gaps in divalent hexaborides. *Phys Rev Lett* 89: 157601.
45. Mori T, Otani S (2002) Ferromagnetism in lanthanum doped CaB_6: Is it intrinsic? *Solid State Commun* 123:287–290.